Green Chemistry

PAPER

View Article Online
View Journal

Cite this: DOI: 10.1039/c9gc04358f

Superhydrophobic nickel/carbon core–shell nanocomposites for the hydrogen transfer reactions of nitrobenzene and N-heterocycles†

Shaofeng Pang, *[a,b] Yujing Zhang,[c] Qiong Su,[a,b] Fangfang Liu,[a,b] Xin Xie,[a,b] Zhiying Duan,[a,b] Feng Zhou,[d] Ping Zhang[a,b] and Yanbin Wang*[a,b]

In this work, catalytic hydrogen transfer as an effective, green, convenient and economical strategy is for the first time used to synthesize anilines and N-heterocyclic aromatic compounds from nitrobenzene and N-heterocycles in one step. Nevertheless, how to effectively reduce the possible effects of water on the catalyst by removal of the by-product water, and to further introduce water as the solvent based on green chemistry are still challenges. Since the structures and properties of carbon nanocomposites are easily modified by controllable construction, a one step pyrolysis process is used for controllable construction of micro/nano hierarchical carbon nanocomposites with core–shell structures and magnetic separation performance. Using various characterization methods and model reactions the relationship between the structure of Ni@NCFs (nickel–nitrogen-doped carbon frameworks) and catalytic performance was investigated, and the results show that there is a positive correlation between the catalytic performance and hydrophobicity of catalysts. Besides, the possible catalytically active sites, which are formed by the interaction of pyridinic N and graphitic N in the structure of nitrogen-doped graphene with the surfaces of Ni nanoparticles, should be pivotal to achieving the relatively high catalytic performance of materials. Due to its unique structure, the obtained Ni@NCF-700 catalyst with superhydrophobicity shows extraordinary performances toward the hydrogen transfer reaction of nitrobenzene and N-heterocycles in the aqueous state; meanwhile, it was also found that Ni@NCF-700 still retained its excellent catalytic activity and structural integrity after three cycles. Compared with traditional catalytic systems, our catalytic systems offer a highly effective, green and economical alternative for nitrobenzene and N-heterocycle transformation, and may open up a new avenue for simple construction of structure and activity defined carbon nanocomposite heterogeneous catalysts with superhydrophobicity.

Received 21st December 2019,
Accepted 15th February 2020

DOI: 10.1039/c9gc04358f

rsc.li/greenchem

Introduction

Arylamines, especially anilines and N-heterocyclic aromatic compounds, have considerable importance in a variety of industrial processes, including pharmaceuticals, dyes, pesticides and so forth.[1–4] In view of the catalytic synthesis of anilines and N-heterocyclic aromatic compounds, great progress has been made in the past decade.[5–8] Among the different methods, catalytic reduction of nitrobenzene to anilines or catalytic oxidation of N-heterocycles to quinolines and indoles, which occur under relatively mild reaction conditions and with simple facilities compared to other methods, as important routes for the synthesis of anilines or quinolines and indoles, constitute fundamental processes in organic synthesis (Scheme 1).[9–15] However, both catalytic reduction and catalytic oxidation require the addition of external reagents (*i.g.*, reductants or oxidants), which often suffer from several drawbacks, such as relatively low atomic economy and undesirable by-products. In particular, these two kinds of reactions are performed in different catalytic systems, which will further increase the cost of the whole reaction.[13,16,17] Hence, how to achieve the catalytic preparation of anilines, quinolines and indoles with higher atom economy by the concept of green chemistry continues to attract scientific interest.

[a]*Chemical Engineering Institute, Northwest Minzu University, Lanzhou, 730030, P. R. China*
[b]*Key Laboratory of Environmental Friendly Composite Materials and Biomass in Universities of Gansu Province, Northwest Minzu University, Lanzhou, 730030, P. R. China*
[c]*College of Chemistry and Chemical Engineering, Northwest Normal University, Lanzhou 730070, P. R. China*
[d]*Dalian National Laboratory for Clean Energy, Dalian Institute of Chemical Physics, Chinese Academy of Sciences, 457 Zhongshan Road, Dalian 116023, P. R. China*
†Electronic supplementary information (ESI) available. See DOI: 10.1039/c9gc04358f

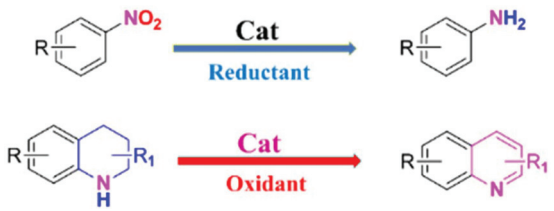

Scheme 1 Catalytic synthesis of anilines and N-heterocyclic aromatic compounds.

Generally, there are two concepts described in green chemistry: atom economy and chemical specificity.[18] Catalytic hydrogen transfer, as a much safer and more environmentally benign process, adopts a privileged position in many green chemistry processes due to the clean transformation and higher atom economy of the overall reaction, especially in the methodological tool box of the fine chemical industry and organic laboratories.[19,20] Till now, a considerable variety of electrophiles (alkanes, alcohols, and amines) have been obtained in good to excellent yields and water is generated as one of the by-products by the catalytic hydrogen transfer reaction under homogenous or heterogeneous conditions.[21–27] Recently, our group has carried out research on the preparation of biphenylamine and triphenylamine by the reaction of nitrobenzene and cyclohexanone *via* a catalytic hydrogen transfer process. The mechanistic studies prove that this reaction starts with the transfer hydrogenation reaction between nitrobenzene and cyclohexanone to generate anilines.[28] Motivated by this, therefore, it also should be interesting to build up a bridge between the hydrogenation of nitrobenzene and the oxidation of N-heterocycles for the preparation of anilines and quinolines or indoles *via* a catalytic hydrogen transfer strategy (Scheme 2).

Notably, on account of the fact that the hydrogen transfer process is usually accompanied by the production of water as one of the by-products, the formation of water may affect the performance of the catalytic materials.[19,29,30] Thus, we consider that the strong water repelling ability can promote the desorption of water from the catalyst surface, effectively reduce the possible effects of water on the catalyst, and increase the adhesion of the catalyst to less polar reactants (*i.g.*, nitrobenzene and N-heterocycles), so as to decrease the mass transfer resistance on active sites, achieving relatively high catalytic activities and selectivities. As mentioned above, we propose the idea of the construction of superhydrophobic materials as efficient catalysts for this reaction with the removal of the by-product water and further introduction of water as the solvent based on the 12 principles of green chemistry.[31]

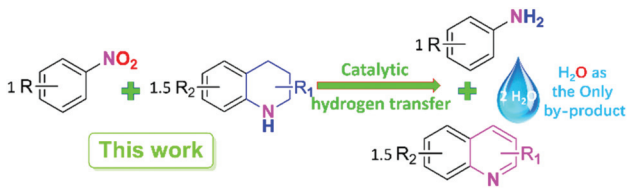

Scheme 2 One-step catalytic synthesis of anilines and quinolines or indoles.

The superhydrophobicity of a material surface is an important property, particularly in catalysis; the special wettability properties of catalysts played a key role in heterogeneous catalytic reactions. To date, a number of construction protocols for fabrication of catalytic materials with superhydrophobic surfaces have been explored. However, to the best of our knowledge, most of these methods and techniques are costly and time-consuming, and often involve complicated multistage processes.[32–36] Thus, a low cost and simple method for the preparation of catalysts with superhydrophobicity is still urgently desired.

As is well known, carbon nanocomposites as highly efficient and green catalytic materials, with well-defined molecular structures have been investigated for many important chemical transformations.[37–39] More importantly, the structures and performances of this class of materials are easy to modify by controllable construction based on the structural design.[40] Therefore, combining the structural design with controllable construction may be a low cost and simple strategy for preparing the superhydrophobic catalysts with both micro–nano hierarchical structure and catalytic active sites. Nevertheless, it is still a big challenge to fabricate both a desirable overall structure and catalytically active sites in one step. According to the survey, we also observed that superhydrophobic carbon nanocomposite catalytic materials and their use in the catalytic hydrogen transfer reaction have rarely been studied. However, very recently, we described the preparation of conductive superhydrophobic nanocarbon materials from waste wheat straw *via* controllable construction, where their structures and hydrophobicity can be tuned efficiently by the annealing temperature.[41] Based on this, and according to the basic principles of the coordination of transition metals to PVP (polyvinyl pyrrolidone),[42] herein we present a simple and low-cost strategy to convert a mixture of PVP/nickel nitrate to catalytic materials with a hierarchical structure composed of micro-flakes and nano-globules in one facile step (Scheme 3), namely, the target materials were formed by controllable carbonization after mixing the PVP solution with nickel nitrate and removing water from the mixture, where the release rate of gas in the pyrolysis process of PVP/nickel nitrate is the key factor to determine the hydrophobicity of materials. Furthermore, the size of nano-globules with core–shell structures of the final solid carbons can be adjusted by changing the annealing temperature in the initial stage. Notably, in our previous work, nickel can be considered as an essential element to generate the active sites of catalysts and exhibited many advantages in the hydrogen transfer process because of its great magnetism and basic attributes, such as reusability, simplicity and certain stability.[43,44] Thus, nickel nitrate is not only used as the catalytically active component, but also as the foaming agent for the preparation of carbon nanocomposite catalytic materials with hydrophobicity. Crucially, according to various characterization methods and model reactions used to

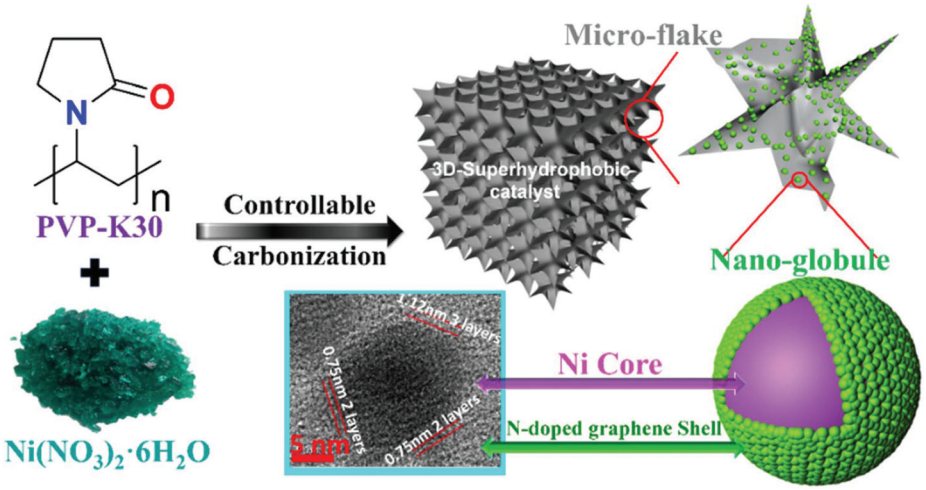

Scheme 3 Preparation of Ni@NCF-700 with a hierarchical structure through controllable carbonization.

investigate the relationship between the structure of Ni@NCFs (nickel–nitrogen-doped carbon frameworks) and the catalytic performance, the excellent catalytic performance of the samples can be assigned to the hydrophobicity of catalysts and the possible catalytically active sites, which are composed of Ni nanoparticles with pyridinic N and graphitic N in the structure of the nitrogen-doped graphene shell. In particular, a positive correlation was found between the catalytic performance and hydrophobicity of catalysts, where Ni@NCF-700 shows superhydrophobicity with a WCA (water contact angle) of up to 160°, and excellent catalytic performance for the reaction of nitrobenzene and N-heterocycles to synthesize anilines and N-heterocyclic aromatic compounds in the aqueous phase.

Experimental section

Typical procedure for Ni@NCF-700 preparation

A mixture of 1.0 g of PVP (K30) and $Ni(NO_3)_2{\cdot}6H_2O$ (1.08 g, 3.7 mmol) was added to deionized water (30 mL) and agitated until complete dissolution. Subsequently, the mixture was transferred into a 150 mL balloon flask and kept at 90 °C *in vacuo* to remove the water. The obtained solid material was further dried at 80 °C overnight. Then, the sample was placed in the feed pipe and pyrolyzed under a N_2 flow (99.999%) at 700 °C for 1 h (heating rate: 4 °C min^{-1}), after which the reactor was cooled to room temperature under the N_2 flow, and 0.6 g Ni@NCF-700 was obtained. In contrast, different samples were prepared with the same procedure but at different annealing temperatures, and denoted as Ni@NCF-600, Ni@NCF-800 and Ni@NCF-900, respectively. The other catalysts (Ni@1/2-NCF-700, Ni@2-NCF-700 and NCF-700) were prepared with the same procedure but with different amounts of nickel nitrate, such as $Ni(NO_3)_2{\cdot}6H_2O$ (0.75 g, 1.85 mmol), (3 g, 7.4 mmol) and no nickel nitrate.

Typical procedures for aniline and quinoline synthesis and catalyst recycling

0.5 mmol (61.5 mg) nitrobenzene, 0.75 mmol (99.9 mg) 1,2,3,4-tetrahydroquinoline, 50 mg catalyst and 2 mL H_2O were added into a 15 mL pressure tube equipped with a magnetic stirrer. Subsequently, the pressure tube was purged with N_2 by using a long needle for three minutes and then quickly sealed with a Teflon thread plug. The pressure tube was placed into an aluminium block, heated to 145 °C (reaction temperature) and stirred for 18 h. The pressure in the tube reached 0.35 MPa during the reaction. After the reaction, the external standard method was used for quantitative analysis. The pressure tube was cooled to room temperature, and 70 mg biphenyl as the external standard and 10 mL ethanol as the solvent were added for quantitative analysis by GC-FID (Agilent 6890A) with a 29 m HP-5 column. For GC-MS analysis, the Agilent GC-MS-HP5890 instrument was used. The magnetic stir bar covered with the catalyst was taken out directly, washed with ethyl acetate and *n*-hexane, and used for the next run.

Purification procedure

The crude products were subjected to silica gel column chromatography (60, 0.053–0.038 mm supplied by Qingdao Haiyang Chemical and Special Silica Gel Co, Ltd) and eluted with about 75 mL of petroleum ether, followed by petroleum ether/EtOAc (500–200 : 1) to give the corresponding products in good yields.

Results and discussion

In order to understand the correlation between the structure and catalytic performance of catalysts, the corresponding Ni@NCFs were preliminarily studied and investigated by scanning electron microscopy (SEM) and water contact angle (WCA) measurement, as shown in Fig. 1 and the insets. The structures of Ni@NCFs consist of micro-flakes which can be clearly observed. Besides, this kind of microstructure as a

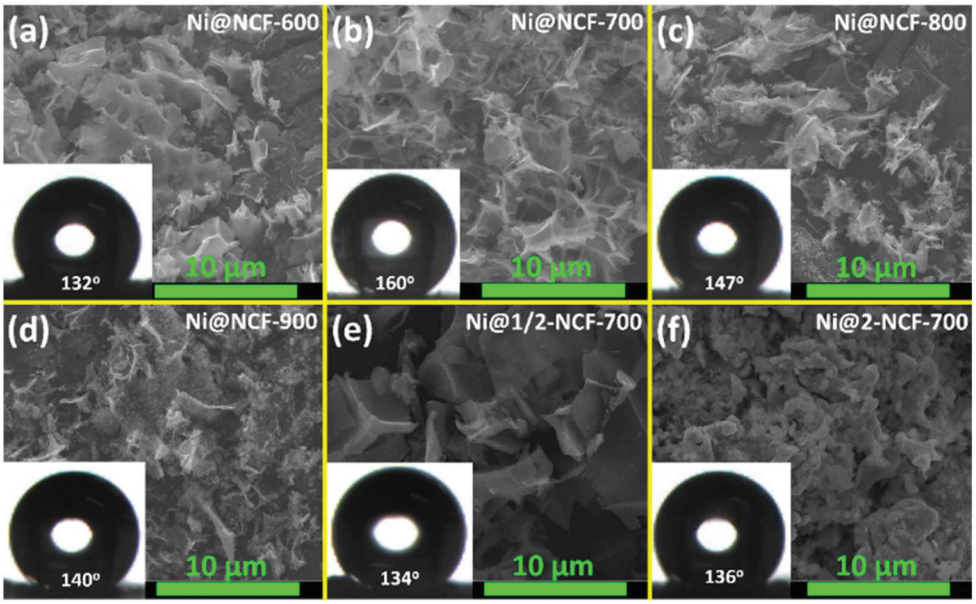

Fig. 1 SEM images of Ni@NCFs at low magnification (original magn. × 15 000, bar = 10 μm). The insets are the corresponding wetting experiments and water contact angle degree.

basic unit structure is made up of a 3D framework, but borders of the 3D framework tend to be fuzzy with the increase of annealing temperature, and even more blurry markedly over 700 °C. It is suggested that the annealing temperature is a critical factor to control the bifurcation process of the carbon skeletons of micro-flakes. Meanwhile, it is noteworthy that the nano-globules gradually become visible with increased annealing temperature as shown in Fig. 1a–d. However, when the use of nickel nitrate as a foaming agent was reduced, the cell walls of micro-flakes became thicker and stronger (Fig. 1e), while when the amount of nickel nitrate was doubled, the microstructure of Ni@2-NCF-700 (Fig. 1f) tightly re-aggregated and formed irregular mass. This phenomenon may be caused by the excessive foaming during the process of the core–shell formation, which might result in hard aggregation of metal particles initially encapsulated in the shell structures.[45,46] In addition, the insets of Fig. 1a–f show the results of wetting experiments performed on a glass substrate using a water droplet of 1 μL. As expected, the water contact angle of Ni@NCF-600 is 132°; the contact angle then continues to increase remarkably to 160° for Ni@NCF-700, which indicates that Ni@NCF-700 has superhydrophobic properties. However, when the annealing temperature rises, the contact angle of Ni@NCF-800 and Ni@NCF-900 decreases obviously, which have a water contact angle of 147° and 140°, respectively. Beyond expectation, Ni@1/2-NCF-700 and Ni@2-NCF-700 also exhibited surface hydrophobicity, with a water contact angle of 134° and 136°, respectively.

As described in Wenzel's theory, the microstructure and nanostructure provide sufficient roughness beneficial to surface superhydrophobicity.[47] However, the size of the fine structure of materials is within the nanometer-scale, and thus can be recognized only at high SEM magnifications. As seen in Fig. 2, high SEM magnifications of Ni@NCF samples confirm the differentiation of their nanostructure. By using various annealing temperatures from 600 °C to 900 °C, the morphology of the resulting Ni@NCFs (Fig. 2a–d) is dramatically different because a number of nano-globules on the surface of materials have gradually become big and more and more apparent. Eventually, nano-globules almost completely covered the micro-flakes (Fig. 2d). However, it should be noted that the surfaces of micro-flakes of Ni@1/2-NCF-700 are covered with tiny nano-burrs, so that it is very difficult to analyze the particle size distribution (Fig. 2e). Besides, for Ni@2-NCF-700, only a few larger particles on micro-flakes were observed clearly (Fig. 2f). In general, the size of nanostructures and the average interval between nanostructures are also crucial factors to achieve the superhydrophobicity of the materials.[48,49] Thus, statistical analysis of the particle size distribution (PSD) was carried out by measuring the number of nano-globules in the insets of Fig. 2. The average nano-globule diameters of Ni@NCF-700, Ni@NCF-800 and Ni@NCF-900 were 49.09 nm, 53.96 nm and 131.56 nm, respectively. A more detailed analysis of the PSD reveals that with the increase of the annealing temperature, the proportion of nano-globule sizes within 25–75 nm decreased from 90.48% to 12%, as well as the interval size within 0–150 nm decreased from 87% to 21%. In contrast, the average interval of nano-globules increased from 118.53 nm to 131.56 nm with increasing annealing temperature; these data of Ni@NCF-700 and Ni@NCF-800 basically obey a normal distribution. In particular, based on these data and previous reports,[41,49] it is clear that the morphology features of Ni@NCF-700 are more suitable for exhibition of superhydrophobic surfaces. As men-

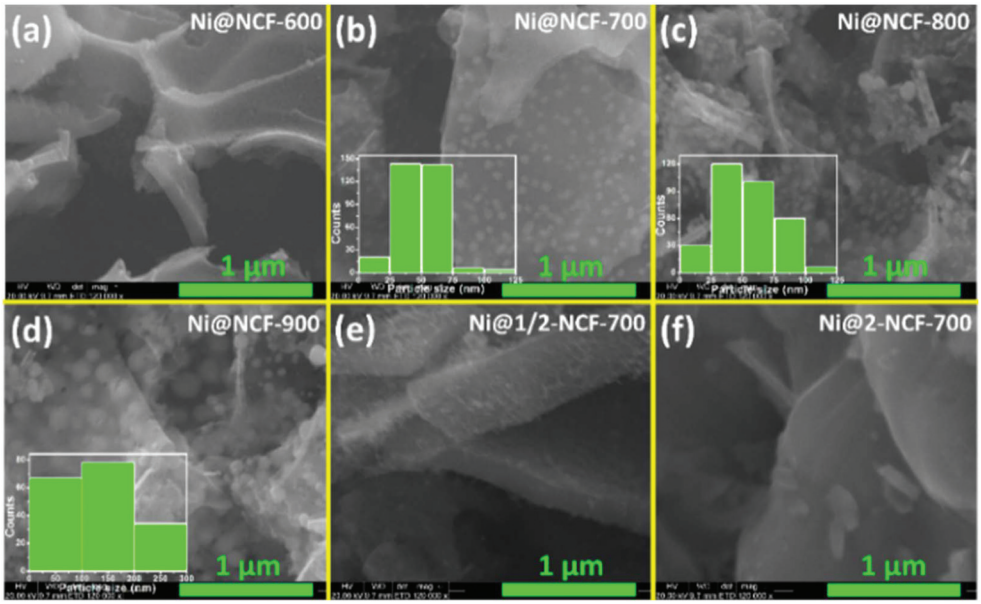

Fig. 2 SEM images of Ni@NCFs at high magnification (original magn. × 120 000, bar = 1 μm). The insets are the corresponding PSD histograms.

tioned above, it should be concluded that the amount of nickel nitrate used as a foaming agent and annealing temperature played key roles in the preparation of superhydrophobic catalytic materials.

In order to verify whether the performance of the catalysts is related to hydrophobicity, annealing temperature, nickel content or specific surface area, we have used the reaction of nitrobenzene and 1,2,3,4-tetrahydroquinoline for the synthesis of aniline and quinoline as a model reaction, and the performances of catalysts were compared with each other. Here in our model reaction, in principle, 1,2,3,4-tetrahydroquinoline can act as a hydrogen donor for nitrobenzene conversion in a process involving hydrogen transfer from tetrahydroquinoline, where 1.5 equivalents of 1,2,3,4-tetrahydroquinoline are needed to transform $-NO_2$ into $-NH_2$ and release two molecules of water. Meanwhile, the corresponding conversions and yields were compared with different solvent systems, which included H_2O and toluene. The detailed data are listed in Table 1. As expected, when using water as a solvent, it was found that the hydrophobicity of catalysts has obvious effects on the catalytic performance; with the increase of the hydrophobicity of the catalyst, the catalytic performance can be improved significantly, and this exhibits the correlation between the two. Ni@NCF-600 with a water contact angle of 132° gives the nitrobenzene conversion at 70% with 68% aniline and 66% quinoline yields (Table 1, entry 1), while 99% nitrobenzene conversion with 97% aniline and 96% quinoline yields was obtained when superhydrophobic Ni@NCF-700 was used as the catalyst (Table 1, entry 2). But when using Ni@NCF-800 (water contact angle of 147°) as a catalyst, not

Table 1 Optimization of the reaction conditions[a]

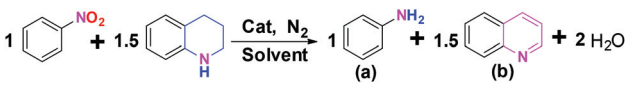

Entry	Catalyst	Solvent	Con.[d] (%)	Con.[e] (%)	Y(a)[f] (%)	Y(b)[f] (%)
1	Ni@NCF-600	H_2O or toluene	70[b]/96[c]	71[b]/96[c]	68[b]/95[c]	66[b]/93[c]
2	Ni@NCF-700	H_2O or toluene	99[b](97[h])/98[c]	99[b](98[h])/99[c]	97[b](95[h])/95[c]	96[b](93[h])/94[c]
3	Ni@NCF-800	H_2O or toluene	77[b]/96[c]	79[b]/98[c]	74[b]/94[c]	71[b]/93[c]
4	Ni@NCF-900	H_2O or toluene	66[b]/74[c]	69[b]/75[c]	62[b]/70[c]	60[b]/66[c]
5	Ni@1/2-NCF-700	H_2O[b]	21[b]	22[b]	14[b]	11[b]
6	Ni@2-NCF-700	H_2O[b]	40[b]	43[b]	34[b]	30[b]
7	Ni@NCF-700	—	11	15	8[g]	7[g]

[a] 0.5 mmol of nitrobenzene, 0.75 mmol of 1,2,3,4-tetrahydroquinoline, 50 mg of the catalyst, 2 mL of solvent, 145 °C (reaction temperature), 18 h, N_2. [b] 2 mL of H_2O as the solvent. [c] 2 mL of toluene as the solvent. [d] Nitrobenzene conversion determined by GC-MS. [e] 1,2,3,4-Tetrahydroquinoline conversion determined by GC-MS. [f] Isolated yield. [g] Determined by GC-FID using biphenyl as the external standard material. [h] The catalyst was used at the 3rd run.

only conversion but also the yield has a significant decrease (Table 1, entry 3). It is noteworthy that Ni@NCF-900 possessed good hydrophobicity with a water contact angle of 140°; however, only 62% aniline and 60% quinoline yields were obtained (Table 1, entry 4), indicating that the catalytic performance may not just be associated with its hydrophobicity. As mentioned above, it can be inferred that the annealing temperature of 900 °C may induce particular changes in the interior structure compared with a relatively lower annealing temperature. In addition, it can be observed obviously that both Ni@1/2-NCF-700 and Ni@2-NCF-700 exhibit lower catalytic performance, which illustrates that a moderate amount of nickel in catalysts is also the key factor to achieve high catalytic performance. As control reactions, we also tested the catalytic activity of the Ni powder (APS 0.25–0.55 micron), NiO (325 mesh) and NCF-700 under the same reaction conditions; Ni powder was used as the catalyst, and gave a relatively lower yield (14% aniline and 12% quinoline). Similarly, a lower yield (9% aniline and 8% quinoline) was also obtained when using NiO as the catalyst. However, no reaction was observed when NCF-700 was used as the catalyst. Thus, the control experiment revealed that Ni and NiO have a certain role in the success of this reaction, but Ni, NiO and NCF-700 cannot be used as catalysts directly. Besides, when the whole catalytic system was subjected to solvent-free conditions, the yields of aniline and quinoline were 8% and 7%, respectively. This phenomenon is a result of solvent-free conditions, which is not a benefit for the diffusion of reactant molecules in the whole catalytic system.[50]

Although the hydrophobicity of catalysts (such as Ni@NCF-600, Ni@NCF-700 and Ni@NCF-800) is related to the catalytic performance in an aqueous solvent system, nevertheless, an important question is whether or not the solvent species influences the model reaction, or catalysts inherently have an appropriate catalytic performance which is not affected by the solvent species. Thus, toluene was chosen as the solvent for the model reaction. Interestingly, although the BET specific surface area of Ni@NCF-700 is 263 m^2 g^{-1} (Table S1†), much larger than those of Ni@NCF-600 (206 m^2 g^{-1}, Table S1†) and Ni@NCF-800 (215 m^2 g^{-1}, Table S1†), both the conversion of nitrobenzene and the yields of aniline and quinoline are excellent and around 95% if Ni@NCF-600, Ni@NCF-700 or Ni@NCF-800 is used as a catalyst. Thus, the catalytic performance of catalysts may not be due to their higher BET surface area. Besides, in consideration of the results of the model reaction with H_2O as a solvent, two conclusions can be drawn: one is water as a solvent has an influence on the properties of the catalysts, so that the catalyst with superhydrophobicity can avoid the effect and exhibit high catalytic performance; the other is that the annealing temperature has some influence on the overall structure of catalysts, but may not have a great influence on the structure of the catalytically active sites of Ni@NCF-600, Ni@NCF-700 or Ni@NCF-800. Besides, as listed in Fig. S1,† the N_2 adsorption–desorption isotherms of Ni@NCF-600 to Ni@2-NCF-700 show a typical IV isotherm shape with a hysteresis loop, suggesting the co-presence of the micro and mesoporous structures. This type of structure could offer channels for mass transfer, in which the surface structure can be penetrated by the less polar molecules so that catalytically active sites can be reached easily.[51,52]

To further recognize the morphology of Ni@NCFs with the influence of different annealing temperatures and the amount of nickel nitrate, the TEM images of Ni@NCFs are also obtained as shown in Fig. S2.† It can be clearly observed that the smaller Ni nanoparticles are well dispersed on the surface of N-doped carbon supports (Fig. S2a and b†), indicating that the introduction of N/O-functional groups may effectively form a stronger metal–support interaction (SMSI) between the metal nanoparticles and N-doped carbon supports. However, the obvious aggregation of Ni nanoparticles can be observed, and the aggregation behavior is gradually intensified with the increasing of annealing temperature (Fig. S2c and d†). Besides, different amounts of nickel have an influence on the morphologies of catalysts. Fig. S2e and f† show the granular structure on the N-doped carbon supports with uneven sizes. In consideration of the results of the model reaction of different catalysts (Table 1), it can be imagined that the presence of smaller Ni nanoparticles and their uniform distribution also should be the key factors for the high activity.

In addition, for Ni@NCF-700, the nano-globule with a core–shell structure was confirmed by HR-TEM, EDX and SAED measurements. Apparently, in Fig. 3a, the HR-TEM image revealed that the Ni nanoparticle was present in metallic crystallite morphology completely covered by a nitrogen-doped graphene shell with 3–5 layers which correspond to a thickness of 1.12–1.87 nm, and the crystal lattice plane distance of Ni (111) (0.21 nm) was measured. Furthermore, the energy dispersive X-ray spectroscopy (EDX) elemental line scans over a randomly selected nano-globule also indicated the formation of a structure with a Ni core and N-doped graphene shell (Fig. 3b and d). These results were further confirmed by the ring-like selected-

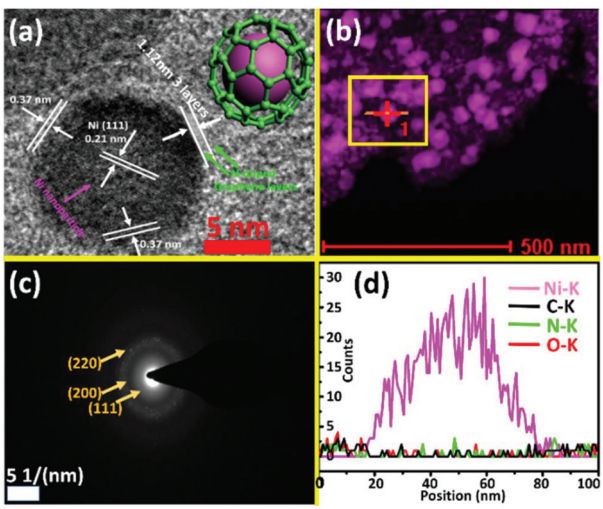

Fig. 3 HR-TEM (a), HAADF (b), the corresponding SAED pattern (c) and the line-scan EDS analysis (d).

area electron diffraction (SAED) patterns (Fig. 3c), indicating that the core–shell structures are polycrystalline. The diffraction rings from inside to outside can also be seen clearly, and the corresponding pattern can be classified as the (111), (200) and (220) planes of Ni in local regions, respectively.

More information can be gained from the XRD characterization results. From Fig. S3,† sharp diffraction peaks of Ni@NCFs centered at 44.507°, 51.846° and 76.370° can be indexed to the Ni (111), Ni (200) and Ni (220) planes, which indicated that the PVP pyrolytical product as a carbon source can effectively reduce nickel oxide during the annealing process. However, the diffraction peak (002) of carbon almost cannot be observed easily, which may be attributed to the fact that there are only small graphite domains present in the samples.[53]

In addition, the FT-IR spectrum was used to investigate the types of functional groups present in the catalysts, and further to understand the possible interaction between the nickel nanoparticles and functional groups. The spectra of NCF-700 and Ni@NCFs were stacked and are displayed in Fig. 4. All the samples containing broad peaks with varying intensities around 3436 cm^{-1} can be assigned to the O–H stretching vibration due to the presence of moisture in the samples.[54] The absorption peaks at 2924 and 2840 cm^{-1} are consistent with the C–H_X stretching vibrations, such as the asymmetric and symmetric CH, CH_2 or CH_3 stretching.[55] The peak at 2348 cm^{-1} ascribed to the C–O bonds and the features at 1743 cm^{-1} are consistent with the vibrational modes of multi-walled carbon nanotubes, which usually existed in carbon materials prepared by the *in situ* doping process with high annealing temperature.[56,57] Most notable for Ni@NCF-900, the intensities of the peaks due to the C–H_X and C–O bonds are enhanced, which demonstrated that the high annealing temperature leads to an increase of the defect degree of the materials and simultaneously induces a strong IR activity.[58,59] Notably, for NCF-700, the mixed stretching mode of the C=N and C=C groups appears at 1621 cm^{-1}. However, the absorption bands of the C=N and C=C groups in Ni@NCFs have been shifted to a lower wavenumber and around at 1548 cm^{-1},[60–62] especially for Ni@NCF-900, this shift is most obvious. It can be inferred that mutual interactions between these functional groups in materials and the surface of the nickel nanoparticles may take place.[54,63] Additionally, a broad peak appeared between 1000 cm^{-1} and 1500 cm^{-1} which can be attributed to the overlap of bands, including the C–N and N–CH_3 bonds at 1250 and 1372 cm^{-1}, the bands of the C=C stretching (1460 cm^{-1}), and the asymmetric and symmetric C–O (1116 cm^{-1}) stretching in the C–O–C group (1053 cm^{-1}), *etc.*[63] In particular, it was difficult to further observe the stretching vibration of NiO at 678 cm^{-1}.[54] This result indicates that the nickel species in catalysts is in the form of metallic nickel, which also corroborates with the XRD results.

To further reveal the structure of the support and shell, which are composed of N-doped graphene, and the role of nitrogen doping in modifying the structure of carbon materials, a detailed Raman study on Ni@NCFs was carried out. As shown in Fig. 5, evidently, there are two intense peaks

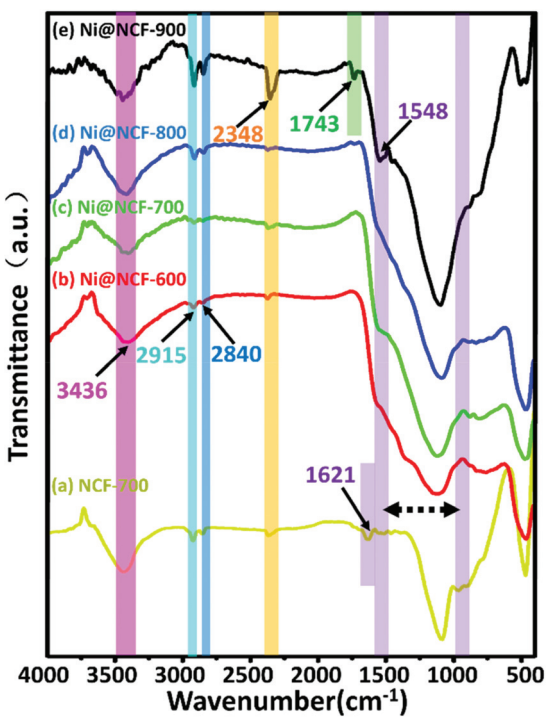

Fig. 4 FT-IR spectra of Ni@NCFs and NCF-700.

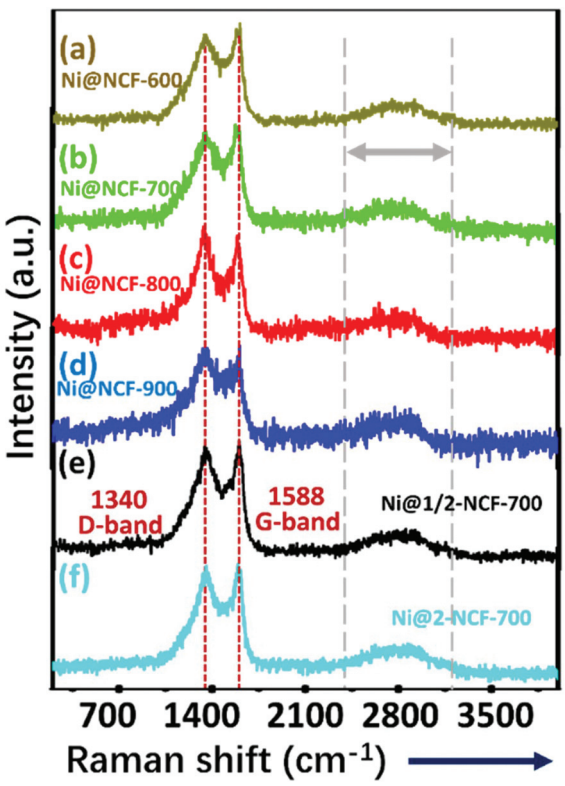

Fig. 5 Raman spectra of Ni@NCFs.

of the Raman spectra for Ni@NCFs. The first one is observed at approximately 1340 cm^{-1} for a well-defined D band, which can be attributed to the multiple overlapping peaks due to the disorder and a large number of obvious defects of the carbon crystallites, including the bands of C–N and C═N vibration at around 1280 cm^{-1} and 1400 cm^{-1}, and the D band of graphene.[64,65] The second peak at around 1588 cm^{-1} is assigned to the G band, which might be caused by the doubly degenerate zone center E_{2g} mode.[41] Furthermore, for Ni@NCF-600, Ni@NCF-700, Ni@NCF-800 and Ni@NCF-900, the ID /IG ratio (peak area) is 2.2, 2.9, 3.4 and 4.6, respectively, which showed that graphitization of the sample is decreased but the defect degree is increased as a result of the increase of annealing temperature. These results are in good accord with the FT-IR results above. In addition, the I_D/I_G ratios (peak area) for Ni@1/2-NCF-700 and Ni@2-NCF-700 are 2.5 and 3.1, respectively; these results suggested that although the reduction mechanisms may be the same, there can be a possible effect for the defect degree of the sample as the amount of metallic oxide increases. Notably, a broad 2D band of Ni@NCFs was observed clearly at around 2800 cm^{-1}, revealing the typical Raman characteristics for few layers of graphene sheets with abundant defects.[66] These results are consistent with the literature and thus explain why Ni@NCF-600, Ni@1/2-NCF-700 and Ni@2-NCF-700 are without an obvious micro–nano hierarchical structure but possess good hydrophobicity; for example, Koratkar *et al.* have reported that with the increasing number of graphene layers, the contact angle of water should increase, due to the fact that the adsorption energy decreases monotonically with the increasing number of graphene layers and causes an increase in the water contact angle.[67]

Normally, using nitrogen-containing organic matter as the precursor, through the *in situ* doping process one can achieve N-doped carbon materials with a homogeneous elemental distribution at controlled temperature, and they always contain N, C, H and O as the main elements.[68,69] In particular, a stronger metal–support interaction (SMSI) can occur between the nitrogen or oxygen functional groups of N-doped carbon materials and metal nanoparticles, which can strongly influence the catalytic performance in specific reactions.[28,70] Thus, to preliminarily reveal the relationship between the amount of N, C, H and O in catalysts and the annealing temperature, elemental analyses of Ni@NCFs with different annealing temperatures are conducted after completing the carbonization process. The elemental analysis of Ni@NCF-600 showed the presence of ~4.09 wt% nitrogen, ~40.83 wt% carbon, ~1.11 wt% hydrogen, and 4.96 wt% oxygen (Table 2, entry 1). Nitrogen content, as very important information, is one of the characteristics of the signal for the content of nitrogen functional groups in N-doped carbon materials. However, the nitrogen, hydrogen and oxygen content obviously reduced with the increasing annealing temperature during the carbonization process. The elemental analysis showed that Ni@NCF-700 contains nitrogen (~2.83 wt%), carbon (~45.42 wt%), hydrogen (~0.59 wt%) and oxygen (~1.03 wt%) (Table 2, entry 2). When the annealing temperature rises to 900 °C, Ni@NCF-900 is obtained with ~0.41 wt% nitrogen, ~46.87 wt% carbon, ~0.13 wt% hydrogen, and ~0.47 wt% oxygen (Table 2, entry 4). In consideration of the results of the model reaction (Table 1), it can be imagined that a suitable amount of the nitrogen functional group and the surface of Ni nanoparticles may form the appropriate catalytically active sites, so as to achieve a high catalytic performance from the catalyst. However, nitrogen-doped materials are a complex system because of the coexistence of various nitrogen and oxygen functional groups, and which type of functionality is responsible for the electronic interaction and further form catalytic activity sites are still undefined. Thus, XPS tests have been used to confirm the relationship between the chemical environment and different annealing temperatures of the samples.

Table 2 EA analysis results of different catalysts[a]

Entry	Catalyst	N	C	H	O	Ni[b]
1	Ni@NCF-600	4.09	40.83	1.11	4.96	49.01
2	Ni@NCF-700	2.83	45.42	0.59	1.03	50.13
3	Ni@NCF-800	1.01	46.77	0.39	0.76	51.07
4	Ni@NCF-900	0.41	46.87	0.13	0.47	52.12

[a] Elemental analysis (N, C, O and H, wt%) of the samples was carried out on a Vario EL microanalyzer. [b] The loadings of all catalyst samples were determined by ICP-AES.

Typical XPS survey scans of the catalysts are shown in Fig. S4,† which indicate that the samples consisted of C, N, O, and Ni as the main elements. The high resolution C 1s spectrum can be fitted by two peaks centered at 284.7 and 285.5 eV, where the peak at 284.7 eV is assigned to the C–C of hybridized graphite-like carbon atoms, which indicates that most of the C atoms in the N-doped graphene sheets are arranged in a conjugated honeycomb lattice, and the peak at 285.5 eV is assigned to the formation of the C–N (Fig. 6).[53,71] In addition, the shifting with the already existing peaks of the C 1s spectra is very hard to observe directly with the increase of annealing temperature. Likewise, the C–O functional groups (such as C═O, C–O and O–C═O) are difficult to observe in the higher-binding energy region of the C 1s spectra.[72]

However, the O 1s spectrum of samples can be clearly observed and deconvoluted into three peaks centered at 531.4, 532.4, and 533.8 eV (Fig. 7, left). Based on the reports about the O 1s spectra of atomic oxygen and referring to the XPS C 1s spectra mentioned above, the O species is assigned to the dissociative atomic oxygen, the oxygen atom association and absorbed water, respectively (Fig. 7a–e).[41,73,74] Moreover, these results of the O 1s spectra are in good agreement with our previous report of carbon-based superhydrophobic materials and also with DFT-calculations.[75] Notably, in contrast to the O 1s spectra of NCF-700, no obvious O 1s binding energy shift can be seen in other samples when introducing Ni, indicating again that the surface of samples, especially the shell structures, may not contain oxygen functional groups. Thus, as

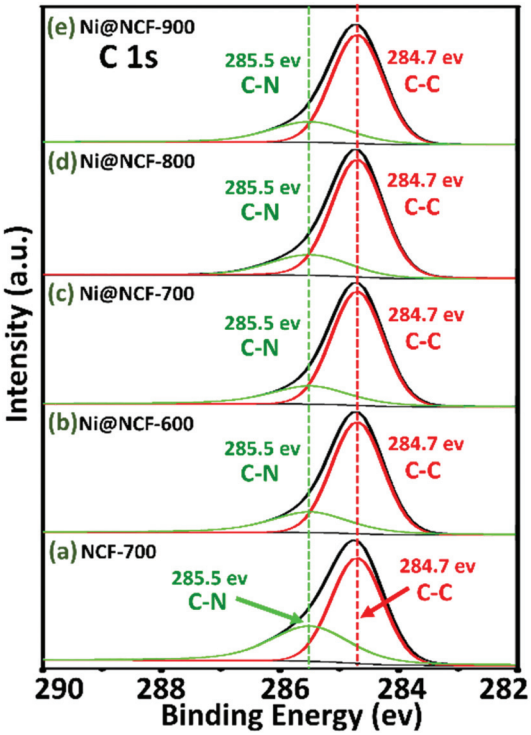

Fig. 6 C 1s spectra of Ni@NCFs and NCF-700.

mentioned above, we can infer that a carbon-based hydrophobic surface with a special structure can trap more air because of not only the trenches of the nano-globules but also the pores on the surface of samples. The N 1s high-resolution XPS spectra of NCF-700 can be deconvoluted into three peaks centered at 398.6, 400.5, and 401.6 eV, corresponding to pyridinic N, pyrrolic N, and graphitic N, respectively (Fig. 7a$_1$).[28,76] Generally, the pyridinic N and pyrrolic N exist on the edges or defect sites in the N-doped graphene sheets, and the graphitic N is within the plane of N-doped graphene; these N species are formed through substituting the nitrogen atom for the carbon atom.[77] Besides, according to the literature, the graphitic N can interact with metal species and plays a key role in dehydrogenation and oxygen reduction due to the stronger π bonds of aromatic rings.[57,70,78–80] Thus, as expected, for Ni@NCF-600 and Ni@NCF-700 (Fig. 7b$_1$ and c$_1$), a noticeable shift of the peaks of the pyridinic N and graphitic N from 398.6 eV and 401.6 eV to 398.3 eV and 401.2 eV occurred after introduction of Ni nanoparticles; these results suggested that the Ni species wrapped into the N-doped graphene shells can effectively increase the electron density of N species, conversely, which also caused the electron-deficient chemical state of Ni nanoparticles. Besides, compared with the N 1s XPS spectra of Ni@NCF-600 and Ni@NCF-700, there is an obvious shift of peaks in the spectra of not only the pyridinic N and graphitic N but also pyrrolic N as the annealing temperature rises from 800 °C to 900 °C, such as Ni@NCF-800 and Ni@NCF-900 (Fig. 7d$_1$ and e$_1$), which strongly implies two facts, one is that the electronic interaction occurred between pyrrolic N and Ni nanoparticles, and the other is that a higher annealing temperature can effectively make N species to interact with Ni nanoparticles more strongly. However, based on the results of the model reaction in water or toluene (Table 1), it can be assumed that the interaction between pyridinic N, graphitic N and the surface of the Ni core might form "the structure of catalytically active sites", which are consistent with the Ni 2p XPS spectra of the samples (Fig. 8).

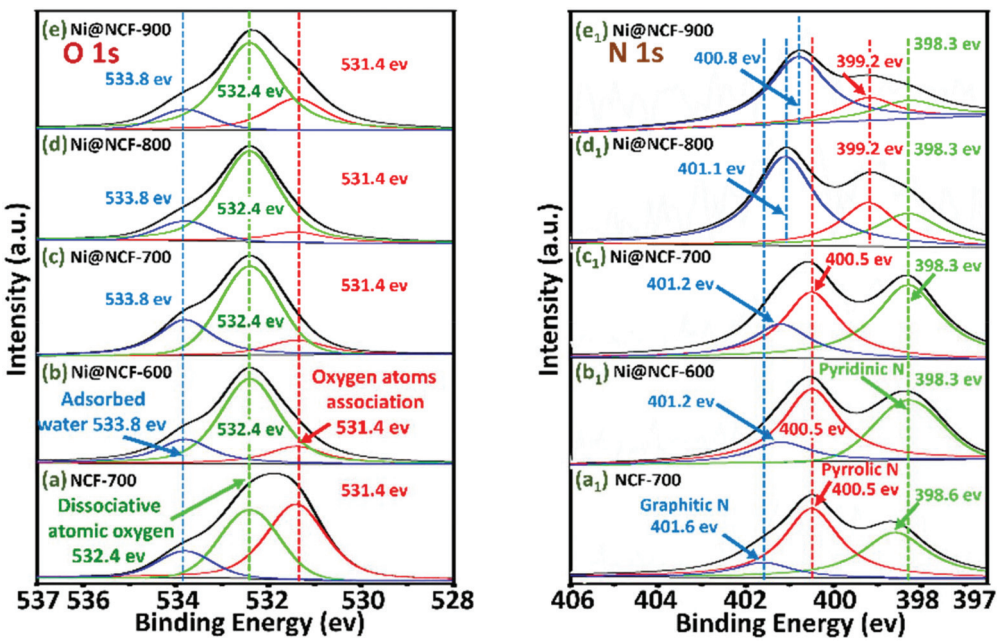

Fig. 7 O 1s (left) and N 1s (right) spectra of Ni@NCFs and NCF-700.

The Ni 2p spectra of Ni@NCF-600 and Ni@NCF-700 are deconvoluted into two groups of peaks (Fig. 8a and b), where two obvious peaks centered at 852.8 and 870.2 eV were observed in the Ni 2p XPS spectra (peak-1), corresponding to the Ni 2p3/2 and 2p1/2, respectively; this mightily proves that the Ni nanoparticles maintain the metallic state as the predominant species in the two samples,[53,81] which is in good accord with the HR-TEM, EDX, SAED and XRD results above. Combined with the results of the N 1s XPS spectra of the two samples (Ni@NCF-600 and Ni@NCF-700) and the model reaction, the peaks at 856.3 eV (Ni 2p3/2) and 873.7 eV (Ni 2p1/2) can be assigned to the Ni species which interacted with the pyridinic N and graphitic N (peak-2), and play the important role of catalytically active sites in the model reaction. Moreover, further increasing the annealing temperature to 800 °C and 900 °C results in new peaks at 861.3 eV (Ni 2p3/2) and 879.2 eV (Ni 2p1/2) (peak-3), which can be observed obviously in Ni@NCF-800 and Ni@NCF-900 (Fig. 8c and d), indicating that the local electronic structure of Ni nanoparticles can be significantly affected by the interaction with not only the pyridinic N and graphitic N but also the pyrrolic N, which is in good agreement with the results of the N 1s XPS spectra. Interestingly, the Ni 2p spectra of Ni@NCF-800 and Ni@NCF-900 are almost identical, including the peak-1, peak-2 and peak-3. However, the catalytic performances of Ni@NCF-800 and Ni@NCF-900 in model reactions with toluene as the solvent are quite different. This phenomenon can be explained by the results of TEM analysis; when the annealing process is conducted at high temperature (*e.g.*, 900 °C), Ni nanoparticles become larger as a result of agglomeration, correspondingly, which could reduce the catalytic performance.

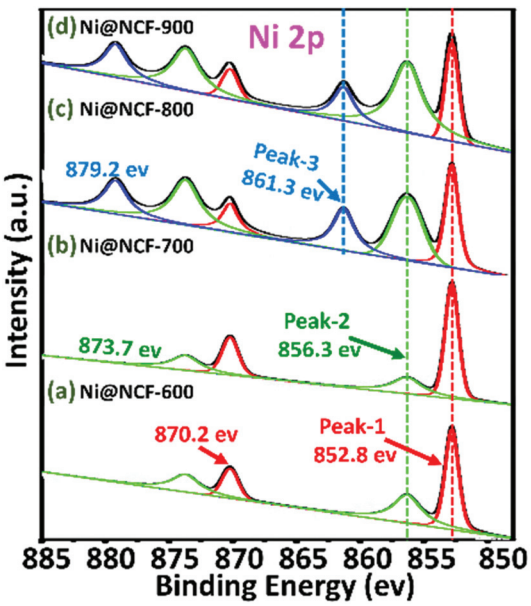

Fig. 8 Ni 2p spectra of Ni@NCFs.

The above results and discussions collectively indicated that the Ni@NCF precursor is directly annealed at high temperature under a nitrogen atmosphere, which can result in a superhydrophobic catalyst with a hierarchical structure composed of micro-flakes and nano-globules (*i.g.*, Ni@NCF-700), where Ni nanoparticles can be encapsulated in an N-doped graphene shell and formed nano-globules with a core–shell structure. During the annealing process, Ni^{2+} cations in the precursor might be completely reduced to Ni nanoparticles by graphene layers, meanwhile pyridinic N and graphitic N in the structure of the nitrogen-doped shell could interact with the surface of Ni nanoparticles for the formation of "the structure of catalytically active sites", so an illustration of the catalyst local structures is given in Scheme 4.

Since Ni@NCF-700 displayed the best activity for the model reaction, it was used in the hydrogen transfer reaction with respect to 1,2,3,4-tetrahydroquinoline with different nitrobenzene compounds under the optimized conditions. As shown in Scheme 5, first, the hydrogen transfer reaction of 1,2,3,4-tetrahydroquinoline with different nitrobenzene compounds was tested (Scheme 5). Notably, substituents on nitrobenzene at the 3 or 4 positions are well tolerated, such as *p*-toluidine (**3b**), *p*-anisidine (**3c**), 3-ethylaniline (**3e**), 4-butyla-

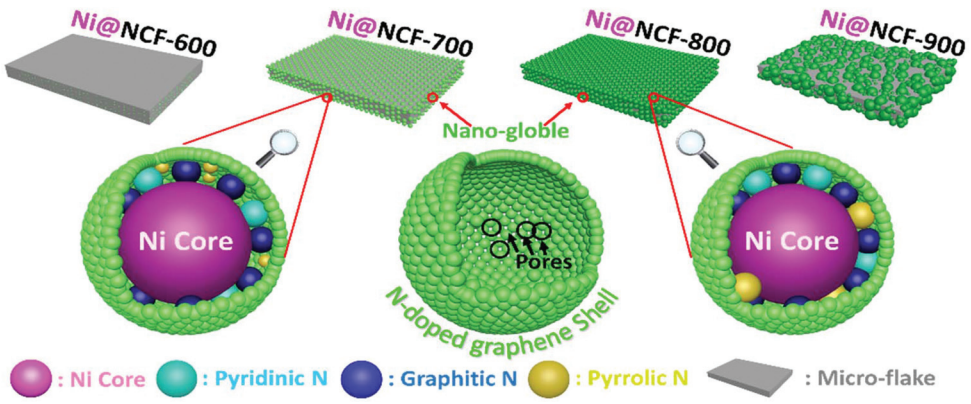

Scheme 4 Pictorial description of Ni@NCFs.

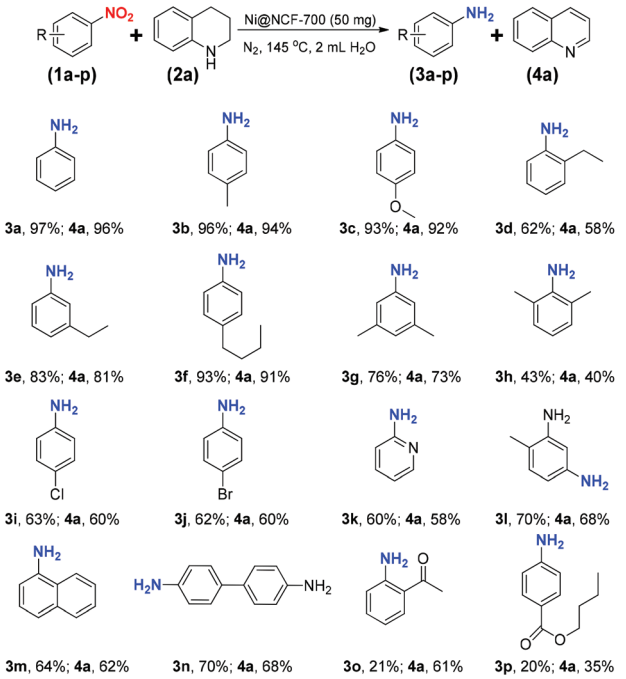

Scheme 5 Results of the hydrogen transfer reaction of 1,2,3,4-tetrahydroquinoline and different nitrobenzene compounds.Conditions: **1** (0.5 mmol), **2** (0.75 mmol), 2 mL of H_2O, 50 mg of catalyst, 145 °C (reaction temperature), 18 h, N_2. All the numbers are isolated yields.

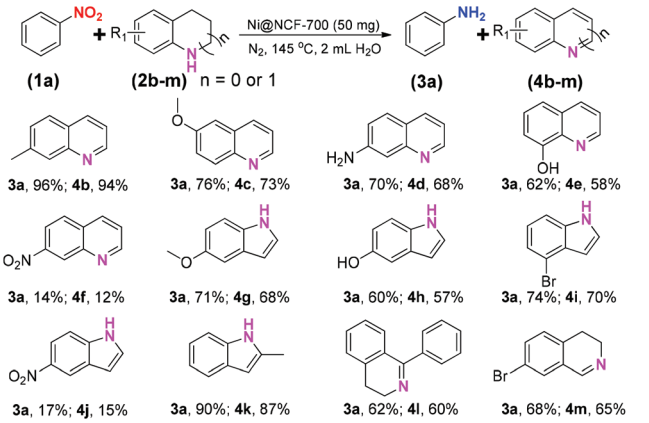

Scheme 6 Results of the hydrogen transfer reaction of nitrobenzene and N-heterocycles. Conditions (n = 0 or 1): **1** (0.5 mmol), **2** (1.5 or 0.75 mmol), 2 mL of H_2O, 50 mg of catalyst, 145 °C (reaction temperature), 18 h, N_2. All the numbers are isolated yields.

niline (**3f**) and 3,5-dimethylaniline (**3g**) which were produced in 96%, 93%, 83%, 93% and 76% yields, respectively. However, more sterically hindered functional groups, such as 2-ethyl (**3d**), 2,6-dimethyl (**3h**), and 2-carbonyl (**3o**), were converted to the corresponding quinolines in 21%–62% yields. Electron-withdrawing groups had a certain influence on the activity of this catalytic system. Thus, 4-chloroaniline (**3i**), 4-bromoaniline (**3j**), 1-naphthylamine (**3m**) and butyl 4-aminobenzoate (**3p**) were obtained with 63%, 62%, 64% and 20% yields. Particularly, a product containing more electron-withdrawing groups such as 1-(2-aminophenyl)-ethanone (**3o**) was isolated in only 21% yield. Meanwhile, it should be pointed out that the reaction does not well tolerate the presence of reducible or hydrolysable functional groups (*i.g.*, carbanyl or ester groups) in the catalytic system, where the production of **3o** and **3p** is accompanied by the production of by-products, such as 1-(2-aminophenyl)ethanol, 1-(2-nitrophenyl)ethanol, 4-aminobenzoic acid or *p*-nitrobenzoic acid, *etc.*, which was detected by GC-MS.

Next, we tested the catalyst by preparing aniline and N-heterocyclic aromatic compounds from nitrobenzene and N-heterocycles. As shown in Scheme 6, the catalyst was also efficient for catalytic hydrogen transfer of nitrobenzene and similar N-heterocycles under 145 °C in water. Gratifyingly, 7-methylquinoline (**4b**) and 2-methyl-1*H*-indole (**4k**) were isolated in yields up to 94% and 87%, respectively. The yield of the other products is about 60–70%. However, products containing more electron-withdrawing groups such as 7-nitroquinoline (**4f**) and 5-nitro-1*H*-indole (**4j**) were isolated with yields of 12% and 15%, respectively, even after a prolonged reaction time. It should be noted that very small amounts of by-products were observed if 7-nitro-1,2,3,4-tetrahydroquinoline was used as the starting material, such as quinolin-7-amine and 1,2,3,4-tetrahydroquinolin-7-amine. As well as indolin-5-amine and 1*H*-indol-5-amine were observed when 5-nitroindoline was used as the starting material. These results indicated that this hydrogen transfer reaction was accompanied by the intra-molecular redox-oxidative reaction.

Finally, the reaction also proceeded successfully with other structurally and electronically diverse nitrobenzene compounds and N-heterocycles (Scheme 7). Clearly, excellent results were obtained and the yields of *p*-toluidine (**3b**) and 7-methylquinoline (**4b**) reached 94% and 92%, respectively. Besides, both *p*-anisidine (**3c**) and 7-methylquinoline (**4b**) were obtained in yields up to 92%. Other nitrobenzene compounds and N-heterocycles with different substituents were also tested, respectively, which gave 50–76% moderate yields towards the corresponding products. However, it should be mentioned that the steric hindrance effect and the electronic effect of substituents had a substantial effect on the reaction. The yields of **3c** and **4c** were 71% and 70%, respectively, when 4-nitroanisole and 6-methoxy-1,2,3,4-tetrahydroquinoline were used as the starting materials, while only 33% **3h** and 35% **4h** was obtained from the reaction of 2,6-dimethyl-1-nitrobenzene and indolin-5-ol. In addition, if nitrobenzene compounds and N-heterocycles containing strong electron-poor groups, *i.e.*, F, were used as the starting materials, almost no desired products were detectable. Nevertheless, this work offers a synthetically powerful and interesting method for catalytic synthesis of anilines and N-heterocyclic aromatic compounds.

Heterogeneous catalysts are used in more than 70% of the industrially relevant processes because catalysts are easily separated and recycled. Compared with other separation processes, the magnetic separation process can effectively reduce

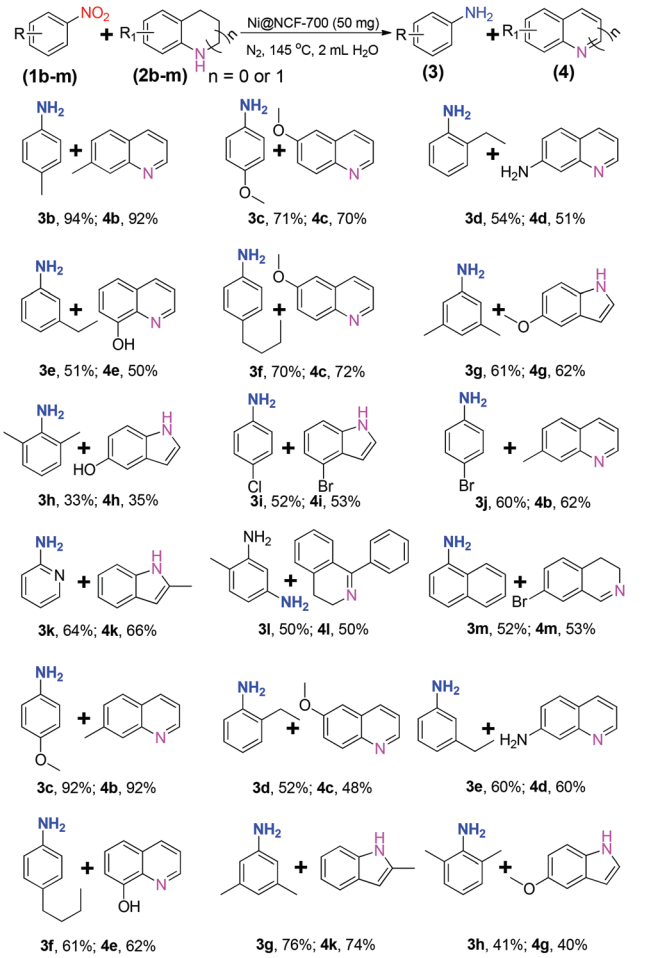

Scheme 7 Results of the hydrogen transfer reaction of nitrobenzene compounds and N-heterocycles. Conditions (n = 0 or 1): **1** (0.5 mmol), **2** (1.5 or 0.75 mmol), 2 mL of H_2O, 50 mg of catalyst, 145 °C (reaction temperature), 18 h, N_2. All the numbers are isolated yields.

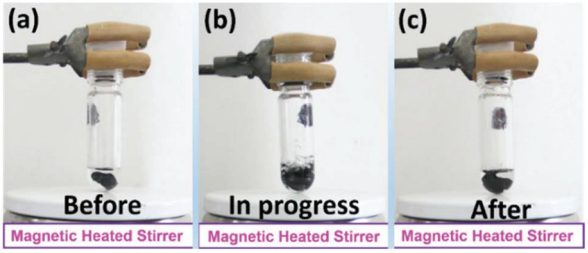

Scheme 8 Digital photos before the reaction started (a), reaction in progress (b) and after the reaction (c).

the production cost;[82,83] thus, it has good application prospects in industrial catalysis. In order to confirm that Ni@NCF-700 shows good magnetic separation performance, the phenomena in the reaction process were carefully observed. When Ni@NCF-700 as a catalyst was added to the solvent (water as the solvent), it floats on the surface because of its superhydrophobicity. However, when a magnetic stir bar was added to the reaction system, it was obvious that the catalyst was rapidly coated on the surface of the magnetic stir bar due to the magnetic properties of the catalyst (see Scheme 8a). During the reaction process, the catalyst wrapped on the surface was dispersed in the solution due to the centrifugal force generated by the high-speed rotation of the magnetic stir bar (see Scheme 8b). Finally, when the reaction was completed, the catalyst was re-coated on the surface of the magnetic stir bar because the magnetic stir bar stopped rotating at a high speed (see Scheme 8c), and then the magnetic stir bar covered with the catalyst could be taken out together and recycled directly after washing with ethyl acetate and n-hexane. Besides, as is known, for a heterogeneous catalyst, the aggregation and leaching of the active metal will be difficult to avoid during the reaction, which often results in deactivation of the catalysts. Thus, the reusability of Ni@NCF-700 in the model reaction was tested. For this purpose, the active material was reused directly 3 times. To our delight, no obvious deactivation was observed. The yield of the desired products was up to 93% (Table 1, entry 2). It is worth noting that the micro–nano hierarchical structure and core–shell structure of Ni@NCF-700 remained intact after the catalyst was used three times, demonstrating the stability of the Ni@NCF-700 architecture (the corresponding morphology is shown in Fig. S5†). All these results suggest that Ni@NCF-700 may have potential applications in the field of fine chemistry and the pharmaceutical industry.

In general, the electrical state of the active hydrogen species (H*) can be polar (hydride and proton, $H^{\delta-}$ and $H^{\delta+}$) and non-polar (radical, $H^{\delta0}$).[84] If H* exists in the electronic neutral state, hydrogen radicals must be involved in the reaction, and the model reaction in the presence of butylated hydroxytoluene (BHT, 0.1 mmol) was investigated. Obviously, in the presence of this radical scavenger, no effect on the catalytic activity was observed, indicating a non-radical hydrogen species-involved reaction path. Furthermore, in order to conduct further discussion on the catalytic mechanism, it was imperative to clarify the reaction process. The reaction of nitrobenzene and 1,2,3,4-tetrahydroquinoline was traced by GC-FID to determine the quantities of the intermediates at different reaction times. The reaction kinetics study has shown that, two hours after the reaction, 0.7 μmol of nitrosobenzene and 0.4 μmol of 1,2-dihydroquinoline were detected. Next, the content of nitrosobenzene and 1,2-dihydroquinoline decreased at 6 h, *i.e.*, 0.34 μmol of nitrosobenzene and 0.21 μmol of 1,2-dihydroquinoline can be observed inside the reaction mixture. As the reaction continued, notably, both nitrosobenzene and 1,2-dihydroquinoline cannot be observed obviously at 14 h. This result shows that the quantities of nitrosobenzene and 1,2-dihydroquinoline decreased remarkably at 14 h, so they fall below the detection limit of GC-FID and cannot be observed, or no longer exist in the reaction system. In light of the aforementioned results, it can be concluded that both nitrosobenzene and 1,2-dihydroquinoline may be the reaction intermediates, as well as that the radical reaction is not involved in

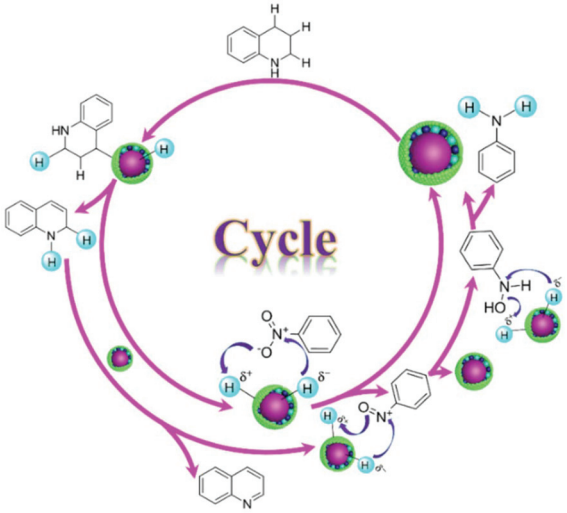

Scheme 9 Proposed reaction mechanism.

this reaction process, which is also consistent with the publications reported by Fukuzumi S, *et al.*[85] Besides, based on the previous reports of catalytic hydrogen transfer, we assumed that the reduction of the nitro group occurred *via* the direct pathway, *i.e.*, the nitro group was first hydrogenated to nitroso and then further to hydroxylamine, and finally to amine; especially, the premise of hydrogenation reactions was to generate the hydride and proton on the catalyst surface.[84,86] Meanwhile, 1,2,3,4-tetrahydroquinoline was dehydrogenated to 1,2-dihydroquinoline, and then sequentially dehydrogenated to quinoline. Just as the basic ligands of transition metal complexes promoted the heterolytic cleavage of H_2 to give metal hydride species,[87] the mechanism involved a cooperation effect between Ni nanoparticles and the N-doped graphene shell as basic sites at the interface of the N incorporated N-doped graphene shell and Ni particles Thus, a possible reaction mechanism is proposed (Scheme 9). First, the dehydrogenation of 1,2,3,4-tetrahydroquinoline to 1,2-dihydroquinoline occurs at catalytically active sites, which promoted 1,2,3,4-tetrahydroquinoline to give Ni–H-species in the metal hydride and split-over H^+ species in N–H^+. Namely, the coordination of 1,2,3,4-tetrahydroquinoline to the Ni core with the assistance of the N-doped graphene shell affords Ni–H-species, followed by β-H elimination on N-doped graphene to give 1,2-dihydroquinoline and N–H^+ species, thus more H^+/H^- pairs were obtained. Then the catalytic dehydrogenation of 1,2-dihydroquinoline to quinoline occurred, which was similar to the dehydrogenation of 1,2,3,4-tetrahydroquinoline to 1,2-dihydroquinoline. Meanwhile, the catalytic hydrogenation of nitrobenzene to nitrosobenzene by the H^+/H^- pairs can then regenerate the catalyst. In the same way, the H^+/H^- pairs will react with nitrosobenzene and generate hydroxylamine. Finally, the reaction occurred between the H^+/H^- pairs and hydroxylamine quickly to give aniline as a product, and the active catalyst would be regenerated for the next cycle.

Conclusions

In summary, we have developed carbon nanocomposite catalytic materials with a unique hydrophobic nature from PVP/nickel nitrate *via* a simple, green and catalyst-free process by controllable construction, in the absence of any expensive catalyst or complex equipment. Their structures and hydrophobicity can be easily modulated by the annealing temperature. In particular, for the unique Ni@NCF-700, the superhydrophobic N-doped graphene shell can behave as a "solid ligand" to cover the Ni core and shows high affinity towards organic substrates in the aqueous phase and excellent catalytic performance in the hydrogen transfer reaction for the synthesis of anilines and N-heterocyclic aromatic compounds in one step. In this catalytic system, the water repelling property of Ni@NCF-700 can remove the by-product water, so as to effectively reduce the possible effects of water on the catalyst, furthermore, which can also further introduce water as a solvent based on the 12 principles of green chemistry. Crucially, a positive correlation was found between the catalytic performance and hydrophobicity of catalysts. Given the above, it is believed that this work should open up a new avenue for green catalytic synthesis of anilines and N-heterocyclic aromatic compounds, and structure and activity defined carbon nanocomposite heterogeneous catalysts with superhydrophobicity for fine chemical synthesis.

Conflicts of interest

There are no conflicts to declare.

Acknowledgements

This research was supported by the National Natural Science Foundation of China (21968032 and 51563022), the Fundamental Research Funds for the Central Universities (31920180043) and the Fundamental Research Funds for Central Universities-Innovation Team Cultivation Project (31920190012 and 31920190015). The Scientific Research Foundation of Northwest Minzu University (xbmuyjrc 201705). Northwest Minzu University's Double First-class and Characteristic Development Guide Special Funds-Chemistry Key Disciplines in Gansu Province (11080316). The Natural Science Foundation of Gansu Province, China (2017GS10863).

References

1 G. Vernin and C. Parkanyi, *Chemistry of heterocyclic compounds in flavours and aromas*, Ellis Horwood Chichester, 1982.
2 Z. Rappoport, *The chemistry of anilines*, John Wiley & Sons, 2007.
3 C. H. McAteer, R. Murugan and Y. V. S. Rao, *Adv. Heterocycl. Chem.*, 2017, **121**, 173–205.

4 P. V. Thanikachalam, R. K. Maurya, V. Garg and V. Monga, *Eur. J. Med. Chem.*, 2019, **180**, 562–612.
5 J. Barluenga, F. Rodriguez and F. J. Fananas, *Chem. – Asian J.*, 2009, **4**, 1036–1048.
6 R. Sharma, P. Kour and A. Kumar, *J. Chem. Sci.*, 2018, **130**, 73.
7 F. Shi and X. Cui, *Catalytic amination for N-alkyl amine synthesis*, Academic Press, 2018.
8 J. Song, Z. F. Huang, L. Pan, K. Li, X. Zhang, L. Wang and J. J. Zou, *Appl. Catal., B*, 2018, **227**, 386–408.
9 E. A. Gelder, S. D. Jackson and C. M. Lok, *Chem. Commun.*, 2005, 522–524.
10 E. Vitaku, D. T. Smith and J. T. Njardarson, *J. Med. Chem.*, 2014, **57**, 10257–10274.
11 Y. Zhang, S. Pang, Z. Wei, H. Jiao, X. Dai, H. Wang and F. Shi, *Nat. Commun.*, 2018, **9**, 1465.
12 L. Sassykova, Y. Aubakirov, S. Sendilvelan, Z. K. Tashmukhambetova, N. Zhakirova and M. Faizullaeva, *Orient. J. Chem.*, 2019, **35**, 22–38.
13 Z. Wei, F. Shao and J. Wang, *Chin. J. Catal.*, 2019, **40**, 980–1002.
14 Y. Wu, Z. Chen, W. C. Cheong, C. Zhang, L. Zheng, W. Yan, R. Yu, C. Chen and Y. Li, *Chem. Sci.*, 2019, **10**, 5345–5352.
15 Q. Liu, S. Tadrent, C. Proust, F. Gomez, A. Khelfa, D. Luart and C. Len, *Chem. Eng. Sci.*, 2020, **211**, 115275.
16 A. B. Charette, *Handbook of Reagents for Organic Synthesis: Reagents for Heteroarene Functionalization*, John Wiley & Sons, 2015.
17 H. Goksu, H. Sert, B. Kilbas and F. Sen, *Curr. Org. Chem.*, 2017, **21**, 794–820.
18 C. J. Li and B. M. Trost, *Proc. Natl. Acad. Sci. U. S. A.*, 2008, **105**, 13197–13202.
19 G. Brieger and T. J. Nestrick, *Chem. Rev.*, 1974, **74**, 567–580.
20 R. A. Johnstone, A. H. Wilby and I. D. Entwistle, *Chem. Rev.*, 1985, **85**, 129–170.
21 S. Bähn, S. Imm, L. Neubert, M. Zhang, H. Neumann and M. Beller, *ChemCatChem*, 2011, **3**, 1853–1864.
22 J. Choi, A. H. R. MacArthur, M. Brookhart and A. S. Goldman, *Chem. Rev.*, 2011, **111**, 1761–1779.
23 A. Corma, J. Navas and M. J. Sabater, *Chem. Rev.*, 2018, **118**, 1410–1459.
24 P. B. Vásquez, T. Tabanelli, E. Monti, S. Albonetti, D. Bonincontro, N. Dimitratos and F. Cavani, *ACS Sustainable Chem. Eng.*, 2019, **7**, 8317–8330.
25 J. Wang, R. Nie, L. Xu, X. Lyu and X. Lu, *Green Chem.*, 2019, **21**, 314–320.
26 M. Xiao, X. Yue, R. Xu, W. Tang, D. Xue, C. Li, M. Lei, J. Xiao and C. Wang, *Angew. Chem., Int. Ed.*, 2019, **58**, 10528–10536.
27 C. Yao, T. Dahmen, A. Gansäuer and J. Norton, *Science*, 2019, **364**, 764–767.
28 S. Pang, Y. Zhang, Y. Huang, H. Yuan and F. Shi, *Catal. Sci. Technol.*, 2017, **7**, 2170–2182.
29 M. Wang, F. Wang, J. Ma, C. Chen, S. Shi and J. Xu, *Chem. Commun.*, 2013, **49**, 6623–6625.
30 R. Labes, C. Mateos, C. Battilocchio, Y. Chen, P. Dingwall, G. R. Cumming, J. A. Rincón, M. J. Nieves-Remacha and S. V. Ley, *Green Chem.*, 2019, **21**, 59–63.
31 P. Anastas and N. Eghbali, *Chem. Soc. Rev.*, 2010, **39**, 301–312.
32 Q. Sun, Z. Dai, X. Meng and F. S. Xiao, *Chem. Soc. Rev.*, 2015, **44**, 6018–6034.
33 J. Jeevahan, M. Chandrasekaran, G. B. Joseph, R. Durairaj and G. Mageshwaran, *J. Coat. Technol. Res.*, 2018, **15**, 231–250.
34 T. Li, J. Wang, F. Wang, L. Zhang, Y. Jiang, H. Arandiyan and H. Li, *ChemCatChem*, 2019, **11**, 1576–1586.
35 P. Sudarsanam, E. Peeters, E. V. Makshina, V. I. Parvulescu and B. F. Sels, *Chem. Soc. Rev.*, 2019, **48**, 2366–2421.
36 Y. Wu, J. Feng, H. Gao, X. Feng and L. Jiang, *Adv. Mater.*, 2019, **31**, 1800718.
37 P. Serp and J. L. Figueiredo, *Carbon materials for catalysis*, Wiley Online Library, 2009.
38 D. S. Su, S. Perathoner and G. Centi, *Catal. Today*, 2012, **186**, 1–6.
39 C. Hu, J. Qu, Y. Xiao, S. Zhao, H. Chen and L. Dai, *ACS Cent. Sci.*, 2019, **5**, 389–408.
40 E. Llobet, *Advanced Nanomaterials for Inexpensive Gas Microsensors*, Elsevier, 2020, pp. 55–84.
41 Y. Wang, D. Zhang, J. Deng, F. Zhou, Z. Duan, Q. Su and S. Pang, *ACS Sustainable Chem. Eng.*, 2019, **7**, 3883–3894.
42 C. Hu, Y. Mu, S. Bai, J. Yang, L. Gao, S. D. Cheng, S. B. Mi and J. Qiu, *Carbon*, 2019, **153**, 609–616.
43 X. Dai, X. Cui, H. Yuan, Y. Deng and F. Shi, *RSC Adv.*, 2015, **5**, 7970–7975.
44 S. Pang and F. Shi, *Tetrahedron Lett.*, 2016, **57**, 5872–5876.
45 R. Ghosh Chaudhuri and S. Paria, *Chem. Rev.*, 2011, **112**, 2373–2433.
46 D. Zhou, S. W. Bennett and A. A. Keller, *PLoS One*, 2012, **7**, e37363.
47 R. N. Wenzel, *Ind. Eng. Chem. Res.*, 1936, **28**, 988–994.
48 X. M. Li, D. Reinhoudt and M. Crego-Calama, *Chem. Soc. Rev.*, 2007, **36**, 1350–1368.
49 G. Wen, Z. Guo and W. Liu, *Nanoscale*, 2017, **9**, 3338–3366.
50 R. A. Sheldon and H. Van Bekkum, *Fine chemicals through heterogeneous catalysis*, John Wiley & Sons, 2008.
51 G. Carja, R. Nakamura, T. Aida and H. Niiyama, *Microporous Mesoporous Mater.*, 2001, **47**, 275–284.
52 G. Zou, H. Hou, J. Hu and X. Ji, *Batteries Supercaps*, 2019, **2**, 712–722.
53 Y. Xu, W. Tu, B. Zhang, S. Yin, Y. Huang, M. Kraft and R. Xu, *Adv. Mater.*, 2017, **29**, 1605957.
54 R. Kumar, R. K. Singh, P. K. Dubey, D. P. Singh, R. M. Yadav and R. S. Tiwari, *Adv. Mater. Interfaces*, 2015, **2**, 1500191.
55 A. Misra, P. K. Tyagi, M. K. Singh and D. Misra, *Diamond Relat. Mater.*, 2006, **15**, 385–388.
56 A. Dillon, T. Gennett, J. Alleman, K. Jones, P. Parilla and M. Heben, Proc. 2000 DOE/NREL Hydrogen program review, 2000, pp. 8–10.

57 X. Cui, Y. Li, S. Bachmann, M. Scalone, A. E. Surkus, K. Junge, C. Topf and M. Beller, *J. Am. Chem. Soc.*, 2015, **137**, 10652–10658.
58 J. Kaufman, S. Metin and D. Saperstein, *Phys. Rev. B: Condens. Matter Mater. Phys.*, 1989, **39**, 13053.
59 Y. Yap, S. Kida, T. Aoyama, Y. Mori and T. Sasaki, *Appl. Phys. Lett.*, 1998, **73**, 915–917.
60 Y. Jia, B. Xiao and K. Thomas, *Langmuir*, 2002, **18**, 470–478.
61 D. P. Dick, H. Knicker, L. G. Ávila, A. V. Inda Jr., E. Giasson and C. A. Bissani, *Org. Geochem.*, 2006, **37**, 1537–1545.
62 Z. Jiang, J. Xie, D. Jiang, X. Wei and M. Chen, *CrystEngComm*, 2013, **15**, 560–569.
63 G. I. Danmaliki, T. A. Saleh and A. A. Shamsuddeen, *Chem. Eng. J.*, 2017, **313**, 993–1003.
64 O. Beyssac, B. Goffé, J. P. Petitet, E. Froigneux, M. Moreau and J. N. Rouzaud, *Spectrochim. Acta, Part A*, 2003, **59**, 2267–2276.
65 I. Y. Jeon, H. J. Choi, M. J. Ju, I. T. Choi, K. Lim, J. Ko, H. K. Kim, J. C. Kim, J. J. Lee and D. Shin, *Sci. Rep.*, 2013, **3**, 2260.
66 S. Y. Lu, M. Jin, Y. Zhang, Y. B. Niu, J. C. Gao and C. M. Li, *Adv. Energy Mater.*, 2018, **8**, 1702545.
67 J. Rafiee, X. Mi, H. Gullapalli, A. V. Thomas, F. Yavari, Y. Shi, P. M. Ajayan and N. A. Koratkar, *Nat. Mater.*, 2012, **11**, 217.
68 W. J. Jiang, J. S. Hu, X. Zhang, Y. Jiang, B. B. Yu, Z. D. Wei and L. J. Wan, *J. Mater. Chem. A*, 2014, **2**, 10154–10160.
69 X. Xu, H. Li and Y. Wang, *ChemCatChem*, 2014, **6**, 3328–3332.
70 W. Shi, B. Zhang, Y. Lin, Q. Wang, Q. Zhang and D. S. Su, *ACS Catal.*, 2016, **6**, 7844–7854.
71 P. Chen, L. K. Wang, G. Wang, M. R. Gao, J. Ge, W. J. Yuan, Y.-H. Shen, A. J. Xie and S. H. Yu, *Energy Environ. Sci.*, 2014, **7**, 4095–4103.
72 D. Yang, A. Velamakanni, G. Bozoklu, S. Park, M. Stoller, R. D. Piner, S. Stankovich, I. Jung, D. A. Field and C. A. Ventrice Jr., *Carbon*, 2009, **47**, 145–152.
73 R. Joyner and M. Roberts, *Chem. Phys. Lett.*, 1979, **60**, 459–462.
74 J. J. Pireaux, M. Liehr, P. Thiry, J. P. Delrue and R. Caudano, *Surf. Sci.*, 1984, **141**, 221–232.
75 A. Boronin, S. Koscheev, K. Murzakhmetov, V. Avdeev and G. Zhidomirov, *Appl. Surf. Sci.*, 2000, **165**, 9–14.
76 W. Yang, J. Li, Q. Fu, L. Zhang, X. Zhu and Q. Liao, *Bioresour. Technol.*, 2017, **241**, 325–331.
77 W. Qiu, J. Jiao, J. Xia, H. Zhong and L. Chen, *Chem. – Eur. J.*, 2015, **21**, 4359–4367.
78 G. Mestl, N. I. Maksimova, N. Keller, V. V. Roddatis and R. Schlögl, *Angew. Chem., Int. Ed.*, 2001, **40**, 2066–2068.
79 V. Strelko, N. Kartel, I. Dukhno, V. Kuts, R. Clarkson and B. Odintsov, *Surf. Sci.*, 2004, **548**, 281–290.
80 C. Chen, J. Zhang, B. Zhang, C. Yu, F. Peng and D. Su, *Chem. Commun.*, 2013, **49**, 8151–8153.
81 L. P. Mei, R. Wang, P. Song, J. J. Feng, Z. G. Wang, J. R. Chen and A. J. Wang, *New J. Chem.*, 2016, **40**, 2315–2320.
82 A. Van Velsen, G. Van der Vos, R. Boersma and J. De Reuver, *Water Sci. Technol.*, 1991, **24**, 195–203.
83 W. Knight and M. Sodhi, *CIRP Ann.*, 2000, **49**, 83–86.
84 C. Zhang, J. Lu, M. Li, Y. Wang, Z. Zhang, H. Chen and F. Wang, *Green Chem.*, 2016, **18**, 2435–2442.
85 S. Fukuzumi and M. Chiba, *J. Chem. Soc., Perkin Trans. 2*, 1991, 1393–1398.
86 Y. Sheng, X. Wang, Z. Xing, X. Chen, X. Zou and X. Lu, *ACS Sustainable Chem. Eng.*, 2019, **9**, 8908–8916.
87 A. Noujima, T. Mitsudome, T. Mizugaki, K. Jitsukawa and K. Kaneda, *Angew. Chem., Int. Ed.*, 2011, **50**, 2986–2989.